Hybrid composite of screen-printed inorganic thermoelectric film and organic conducting polymer for flexible thermoelectric power generator

Ju Hyung We, Sun Jin Kim, Byung Jin Cho[*]

Department of Electrical Engineering, KAIST, 291 Daehak-Ro, Yuseong, Daejeon, Republic of Korea

A B S T R A C T

TEG (Thermoelectric power generator) modules are attractive energy harvesters, as they can deliver electrical output power from the temperature difference of all sorts of things. Recently, growing interests in self-powered wearable mobile electronics provoke the necessity of flexible TEG modules. However, the technology on flexible TEG modules is still at a very early stage. Here we demonstrate flexible high-performance TEG modules using a screen-printed inorganic thermoelectric thick film and organic conducting polymer hybrid composite. By infiltrating the organic conducting polymer, poly(3,4-ethylenedioxythiophene): poly(styrenesulfonate) (PEDOT:PSS), into the micropores of the screen-printed thermoelectric thick film, the flexibility of the module is greatly enhanced without degradation of the output characteristics of the module. This work provides a promising new approach which has the potential to achieve a flexible high-performance TEG module.

© 2014 Elsevier Ltd. All rights reserved.

1. Introduction

TEG (Thermoelectric power generator), which converts waste heat into electricity, is one of the promising energy harvesting devices [1]. The output performance of the TEG module is determined by dimensionless figure-of-merit (ZT). The ZT (or Z) is the ability of a given material to efficiently produce electrical power from thermal gradient [2]. So far, regarding waste heat recovery and harvesting methods, various ways including structure optimization of the module [3] or system [4], organic rankine cycle [5], transcritical rankine cycle [6,7], thermal energy storage integration [8–12], TEG incorporation [13] have been adopted and studied extensively. In recent years, research on flexible TEG module fabrication has attracted great interest due to the potential new market for self-powered wearable mobile electronics [14]. In fact, because many heat sources (human body, power stations, heating systems, motor vehicles, and so on) have arbitrary shapes, a flexible TEG module helps to have better thermal contact with the arbitrary shaped heat sources. However, conventional inorganic TE (thermoelectric) materials such as bismuth telluride (Bi_2Te_3) and antimony telluride (Sb_2Te_3) are unsuitable for flexible TEG modules because of their brittle material properties. To overcome this problem, some groups have proposed organic [15] or organic-based composite materials [16,17] for flexible TEG modules. However, organic-based flexible TEG modules have limitation of low output performance due to their low figure-of-merit ZT value and high contact resistance. Although some organic-metal [18] or organic-inorganic hybrid composite materials [19,20] for flexible TEG modules with improved performance have been proposed, the output performance is still low compared to that of inorganic-based TEG modules.

In this work, flexible high-performance TEG modules using a screen-printed inorganic TE thick film and organic conducting polymer hybrid composite have been realized. In this new approach, the micropores in the screen-printed TE thick film are filled with an organic conducting polymer, PEDOT:PSS, using a spin-coating and infiltration process. Compared to other methods to prepare organic–inorganic hybrid composites, the proposed method is much simpler, cheaper, and mass-production friendly because it is easy to make a large size film quickly. The feasibility of flexible TEG module operation using body heat has also been demonstrated. This work may open a new route to develop flexible high-performance TEG modules.

* Corresponding author. Tel.: +82 42 350 3485; fax: +82 42 350 8565.
  E-mail address: elebjcho81@kaist.ac.kr (B.J. Cho).

Nomenclature

TEG	thermoelectric power generator
TE	thermoelectric
Bi	bismuth
Sb	antimony
Te	tellurium
Ag	silver
Cu	copper
Bi_2Te_3	bismuth telluride
Sb_2Te_3	antimony telluride
PI	polyimide
PEDOT	PSSpoly(3,4-ethylenedioxythiophene): poly(styrenesulfonate)
DMSO	dimethyl sulfoxide
N_2	nitrogen gas
FESEM	field emission scanning electron microscope
SEM	scanning electron microscope
HMS	Hall-effect measurement system
LFA	laser flash apparatus

n	carrier concentration (cm^{-3})
S	Seebeck coefficient ($\mu V\ K^{-1}$)
|S|	absolute value of the Seebeck coefficient ($\mu V\ K^{-1}$)
ZT	figure-of-merit (dimensionless)
Z	figure-of-merit (K^{-1})
R	electrical resistance (Ω)
K	thermal conductance ($W\ K^{-1}$)
L	length of thermoelectric leg (m)
A	area of thermoelectric leg (m^2)

Greek letters

μ	carrier mobility ($cm^2\ V^{-1}\ s^{-1}$)
σ	electrical conductivity ($S\ m^{-1}$)
κ	thermal conductivity ($W\ m^{-1}\ K^{-1}$)
ρ	electrical resistivity ($\Omega\ m$)

Subscripts

p	p-type thermoelectric leg
n	n-type thermoelectric leg

2. Experimental

2.1. Paste synthesis

The paste consists of 75% of metal powders (Bi, Sb, and Te), 2.4% of glass powder, 0.2% of binder, and 22.4% of solvent in their weight compositions. The metal powders have 99.5% purity and the sizes of the metal powder particles are smaller than 5 μm. The powder mixing ratio of Bi and Te was 35:65 while the ratio of Sb and Te was 40:60 in atomic percentage. The pastes were thoroughly mixed for 24 h using ball-mill equipment. The purpose of the glass powder is to increase the adhesion between the substrate and the paste so that the paste would not be delaminated after annealing. The binder maintains the paste's viscosity at a desired level and the solvent is used to mix the powders. The synthesized Bi_2Te_3 paste has viscosity of 40 Pa s while Sb_2Te_3 paste does 65 Pa s.

2.2. Screen-printed thermoelectric thick film formation

The deposition of Bi_2Te_3 (n-type) and Sb_2Te_3 (p-type) TE thick films using a screen-printing technique consists of several steps: screen printing, drying, and annealing. The prepared paste was screen-printed on a flexible PI (polyimide) film substrate by using a 150 mesh screen. After that, the samples were dried at 120 °C for 10 min to remove the solvent. Two-step annealing in a furnace tube was then performed: a binder removal step and a high temperature annealing step. First, the binder removal step was performed at 260 °C for 10 min in a vacuum ambient to remove the organic binder from the paste. The annealing step was then conducted at 450 °C under 110 mm Hg in a N_2 ambient to achieve the best TE properties of the film. This pressure was carefully selected experimentally to avoid oxidation and excess evaporation of Te. When the pressure was close to 1 atm, the film was oxidized. On the other hand, when the pressure was too low, excess evaporation of Te was observed.

2.3. Thermoelectric transport characterization

The morphology of the screen-printed thick films was analyzed by field emission scanning electron microscope (Sirion, FESEM, operating voltage: 10 kV). The Seebeck coefficient was measured by connecting one side of the film to a hot metal block and the other side to a heat sink which is kept at room temperature. By varying and measuring the temperature differences across both sides of the sample and measuring the output voltage, the Seebeck coefficient can accurately be obtained from the slope of the data curve in the plot of temperature difference versus output voltage. The temperature difference and output voltage were measured by a Keithley 2700 equipment simultaneously. The electrical conductivity was measured by the standard Van der Pauw method using a Hall-effect measurement system (Ecopia, HMS-3000) and the thermal conductivity was measured by the standard laser flash method using a Laser Flash Apparatus (NETZSCH, LFA 447).

2.4. Area ratio optimization for the TEG module

To maximize the output power density of a TEG module, the area ratio of p-type and n-type TE legs must be optimized because the TE legs have different electrical and thermal properties. The figure-of-merit Z of a TEG module can be defined as follows:

$$Z = \frac{(S_p - S_n)^2}{R \cdot K}, \tag{1}$$

where S is the Seebeck coefficient, R is the electrical resistance, and K is the thermal conductance of the module. The subscripts 'p' and 'n' represent the p-type and the n-type TE leg. The electrical resistance (R) and thermal conductance (K) are defined as follows:

$$R = \frac{L_p \cdot \rho_p}{A_p} + \frac{L_n \cdot \rho_n}{A_n} \tag{2}$$

$$K = \frac{\kappa_p \cdot A_p}{L_p} + \frac{\kappa_n \cdot A_n}{L_n}, \tag{3}$$

where L is the length, ρ is the electrical resistivity, κ is the thermal conductivity, and A is the area of the TE leg. The figure-of-merit Z is maximized when the product RK is minimized. To minimize RK, the differentiation value of RK respect to A_n/A_p should be zero.

$$RK = \left(\frac{L_p \cdot \rho_p}{A_p} + \frac{L_n \cdot \rho_n}{A_n} \right) \cdot \left(\frac{\kappa_p \cdot A_p}{L_p} + \frac{\kappa_n \cdot A_n}{L_n} \right) \tag{4}$$

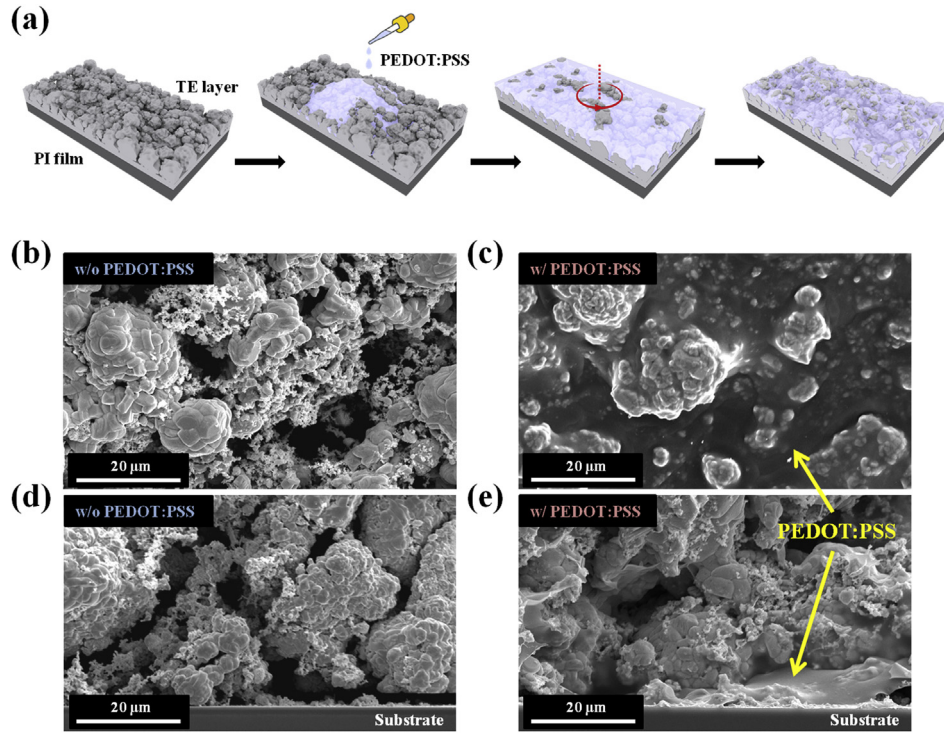Suppose the length of the TE legs is the same ($L_p = L_n$). Then,

Fig. 1. (a) Process flow of PEDOT:PSS infiltration into the screen-printed thermoelectric (TE) thick film. First, a 40 μm-thick TE film was screen-printed on a highly flexible polyimide (PI) film substrate and annealed at 450 °C in a N_2 ambient. The sample was then coated by PEDOT:PSS solution with 5 vol% dimethyl sulfoxide (DMSO) additive and held for 10 min. After that, excess PEDOT:PSS solution was removed by a spinning process at 1500 rpm for 30 s. Finally, the sample was dried at 200 °C for 1 h. Scanning electron microscope (SEM) images show the morphology change of the screen-printed Bi_2Te_3 TE thick film before and after PEDOT:PSS infiltration process. (b) Top view of the film before infiltration. (c) Top view of the film after infiltration. (d) Cross section view of the film before infiltration. (e) Cross section view of the film after infiltration. All scale bars indicate 20 μm.

$$RK = \rho_p \cdot \kappa_p + \rho_p \cdot \kappa_n \cdot \left(\frac{A_n}{A_p}\right) + \rho_n \cdot \kappa_n + \rho_n \cdot \kappa_p \cdot \left(\frac{A_p}{A_n}\right) \quad (5)$$

$$(RK)'\big|_{\frac{A_n}{A_p}} = \rho_p \cdot \kappa_n + \rho_n \cdot \kappa_p \cdot (-1) \cdot \left(\frac{A_p}{A_n}\right)^2 = 0 \quad (6)$$

Therefore, the product RK is minimized when the area ratio satisfies the following condition:

$$\frac{A_n}{A_p} = \sqrt{\frac{\rho_n \cdot \kappa_p}{\rho_p \cdot \kappa_n}} \quad (7)$$

2.5. Device fabrication and characterization

Flexible TEG modules were fabricated using a screen-printed inorganic TE thick film and organic conducting polymer hybrid composite. First, the Bi_2Te_3 film (*n*-type) legs were screen-printed on a flexible PI film and then the Sb_2Te_3 film (*p*-type) legs were printed on the same PI film. The thickness of the TE legs was 40 μm. After the screen printing step, the sample was annealed at 450 °C in a N_2 ambient followed by coating a PEDOT:PSS solution and drying at 200 °C for 1 h. 5 vol% DMSO (dimethyl sulfoxide) solvent was added to the PEDOT:PSS solution to improve the electrical conductivity. Finally, a 10 μm-thick Ag film was screen-printed to electrically connect the TE legs and was annealed at 200 °C for 20 min in a vacuum ambient.

To evaluate the output characteristics of the fabricated TEG module, the exact temperature difference of both sides of the module must be known. In this work, a measuring apparatus using a heater (ramping rate of 5 °C min^{-1}) at the hot side and a cooler (5~30 °C controllable temperature range) at the cold side was used. In order to improve the measurement reliability, the hot side temperature was ramped up, while the cold side temperature was kept constant. The temperature of the cold side was maintained stably at 10 ± 1 °C. The output voltage and temperature difference of the module were measured by a Keithley 2700 equipment simultaneously.

3. Results and discussion

Fig. 1a shows the process flow of PEDOT:PSS infiltration into the screen-printed TE thick film. First, a 40 μm-thick TE film was screen-printed on a highly flexible PI film substrate and annealed at 450 °C in a N_2 ambient. In this work, Bi_2Te_3 for *n*-type and Sb_2Te_3 for *p*-type TE materials were used due to their high TE performance at room temperature. It already has been demonstrated that the TE properties of films prepared by a screen-printing technique are comparable to those of bulk material [21–24]. SEM (Scanning electron microscope) images show the morphology change of the screen-printed Bi_2Te_3 TE thick film before and after the PEDOT:PSS infiltration process. The screen-printed TE thick film has many pores in the film (Fig. 1b and d) due to evaporation of the solvent and organic binder in the paste during the high temperature annealing process. These pores cause relatively low electrical conductivity and weak mechanical strength compared to bulk or thin-film materials. The sample was then coated by a PEDOT:PSS solution with a 5 vol% DMSO (dimethyl sulfoxide) additive and held for 10 min. The DMSO solvent was added to the PEDOT:PSS solution to improve the electrical conductivity [25]. Excess PEDOT:PSS solution was removed by a spinning process at 1500 rpm for 30 s. Finally, the
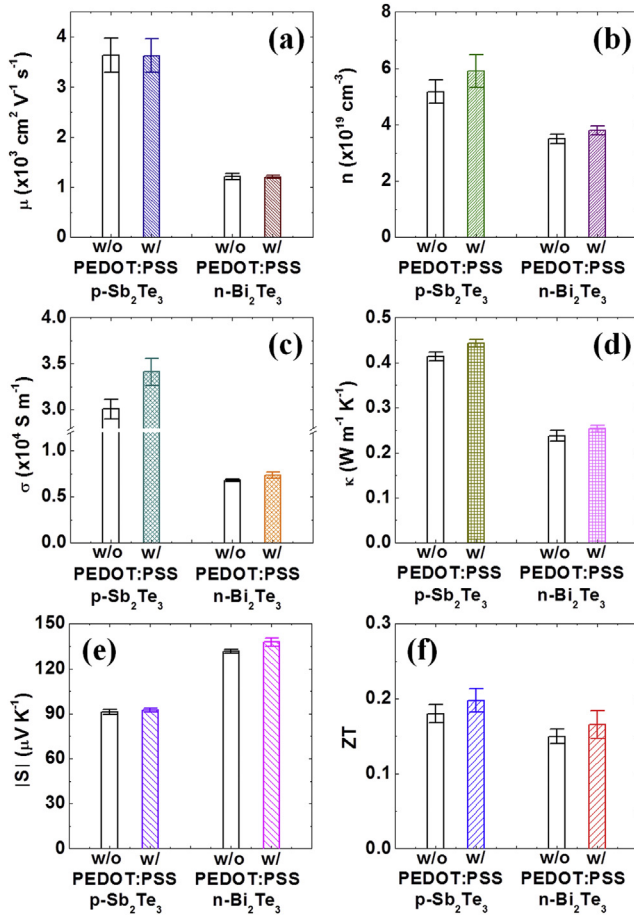
Fig. 2. Thermoelectric properties of screen-printed thermoelectric thick films before and after PEDOT:PSS infiltration process. (a) Carrier mobility (μ), (b) carrier concentration (n), (c) electrical conductivity (σ), (d) thermal conductivity (κ), (e) absolute value of the Seebeck coefficient ($|S|$), and (f) figure-of-merit (ZT) of the samples according as with (w/) or without (w/o) PEDOT:PSS infiltration. The columns indicate the average value and the error bars are standard deviation value of each sample.

sample was dried at 200 °C for 1 h. After the coating process, the PEDOT:PSS infiltrated into almost all empty spaces of the porous film (Fig. 1c and e). Fig. 1e confirms that the PEDOT:PSS fully infiltrated into the entire film with thickness of 40 μm.

Fig. 2 and Table 1 show the TE properties of the screen-printed TE thick films before and after the PEDOT:PSS infiltration process. Fig. 2a and b indicate the changes of the carrier mobility (μ) and carrier concentration (n) of the samples before and after PEDOT:PSS infiltration. The PEDOT:PSS does not affect carrier mobility, but increases the carrier concentration of the screen-printed TE thick films approximately 9~14%. This is due to additional carriers added from the highly conductive PEDOT:PSS filled in the micropores of the TE film. This tendency is found in both n-type Bi_2Te_3 and p-type
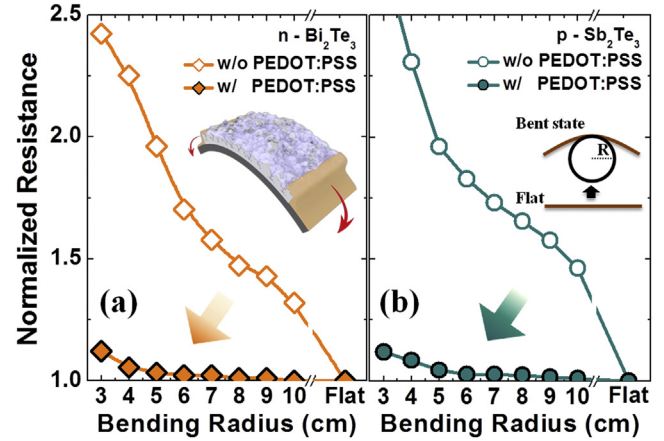

Fig. 3. Resistance changes of the screen-printed thermoelectric (TE) films before and after PEDOT:PSS infiltration process as a function of bending radius. The resistance values were normalized by the resistance of the flat sample. The resistances of unbent Bi_2Te_3 samples with and without PEDOT:PSS infiltration are 9.1 Ω and 9.2 Ω. The resistance of the unbent Sb_2Te_3 samples is 2.0 Ω for both with and without PEDOT:PSS infiltration. (a) Resistance changes of the screen-printed n-type Bi_2Te_3 TE thick films before (open diamonds) and after (filled diamonds) PEDOT:PSS infiltration. (b) Resistance changes of the screen-printed p-type Sb_2Te_3 TE thick films before (open circles) and after (filled circles) PEDOT:PSS infiltration.
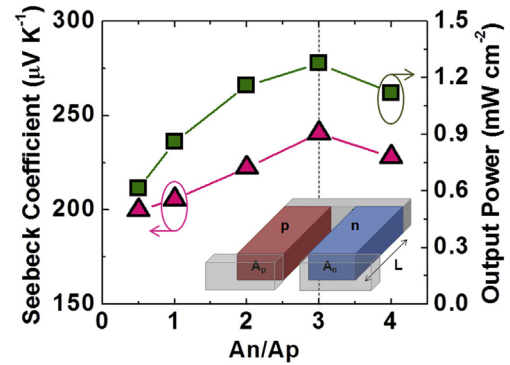

Fig. 4. The Seebeck coefficient (filled triangles) and output power density (filled squares) of the TEG module as a function of different area ratio (A_n/A_p).

Table 2
The Seebeck coefficient and output power density of the TEG module as a function of different area ratio (A_n/A_p).

A_n/A_p	Seebeck coefficient ($\mu V~K^{-1}$)	Output power density ($mW~cm^{-2}$)
0.5	199.9 ± 3.5	0.61 ± 0.02
1.0	205.5 ± 3.6	0.86 ± 0.03
2.0	222.3 ± 3.9	1.16 ± 0.05
3.0	240.5 ± 4.2	1.28 ± 0.05
4.0	228.0 ± 4.0	1.12 ± 0.04

Table 1
Thermoelectric properties of screen-printed thermoelectric thick films before and after PEDOT:PSS infiltration process.

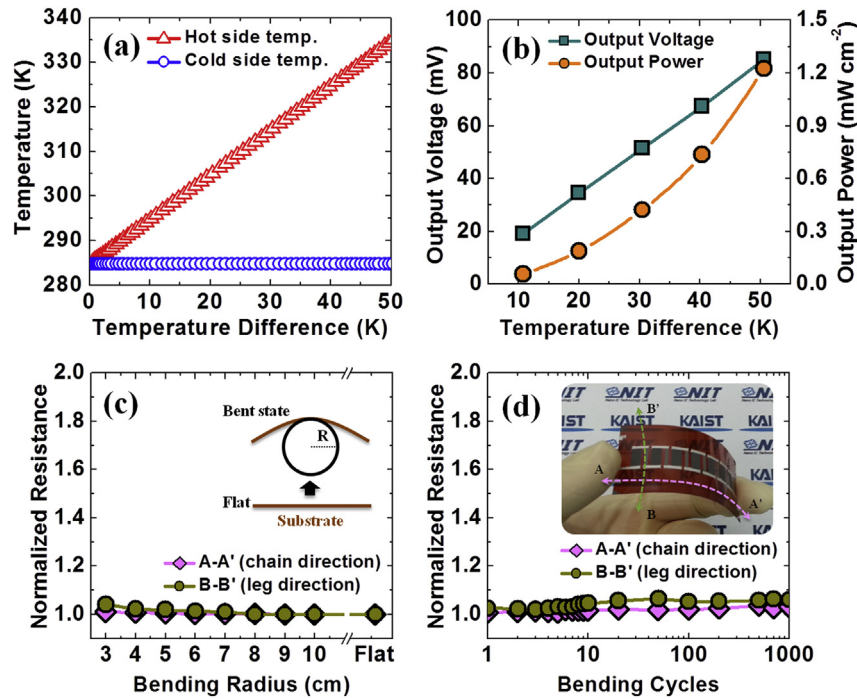| Variables	Sb_2Te_3 film (p-type)		Bi_2Te_3 film (n-type)	
	w/o PEDOT:PSS	w/PEDOT:PSS	w/o PEDOT:PSS	w/PEDOT:PSS
Carrier mobility, μ ($\times 10^3~cm^2~V^{-1}~s^{-1}$)	3.64 ± 0.34	3.63 ± 0.33	1.22 ± 0.06	1.21 ± 0.04
Carrier concentration, n ($\times 10^{19}~cm^{-3}$)	5.17 ± 0.43	5.90 ± 0.58	3.50 ± 0.17	3.80 ± 0.17
Electrical conductivity, σ ($\times 10^4~S~m^{-1}$)	3.01 ± 0.11	3.41 ± 0.15	0.68 ± 0.01	0.73 ± 0.04
Thermal conductivity, κ ($W~m^{-1}~K^{-1}$)	0.41 ± 0.01	0.44 ± 0.01	0.24 ± 0.01	0.25 ± 0.01
Seebeck coefficient, S ($\mu V~K^{-1}$)	91.3 ± 1.6	92.6 ± 1.2	−131.6 ± 1.4	−137.8 ± 2.8
Figure-of-merit, ZT (dimensionless)	0.18 ± 0.01	0.20 ± 0.02	0.15 ± 0.01	0.16 ± 0.01

Fig. 5. Output characteristics of a fabricated flexible thermoelectric power generator (TEG) module. (a) Temperature profiles of the hot side (open triangles) and cold side (open circles) during measurement. (b) Output voltage (filled squares) and output power density (filled circles) as a function of temperature difference. (c) Resistance changes of the module as a function of bending radius in chain direction (A–A', filled diamonds) and leg direction (B–B', filled circles). The internal resistance of the unbent (flat) TEG module is 145.2 Ω. (d) Resistance changes of the module as a function of the number of bending cycles with bending radius of 4 cm.

Sb_2Te_3 TE films. Fig. 2c shows the increase of electrical conductivity (σ) after PEDOT:PSS infiltration, which is the reflection of the carrier concentration increase, as shown in Fig. 2b. However, the increase of the carrier concentration also increases the thermal conductivity (κ) of the samples, as shown in Fig. 2d, because the carrier concentration is directly related to the electronic thermal conductivity. Such trade-off relation between the electrical conductivity and thermal conductivity is often found in TE materials and the PEDOT:PSS infiltration process also shows a similar tendency. However, it should be noted that the change of the carrier concentration by the PEDOT:PSS infiltration process is not high enough to affect the Seebeck coefficient, thus resulting in no observable difference in the absolute value of the Seebeck coefficient ($|S|$) after PEDOT:PSS infiltration (Fig. 2e). Fig. 2f shows the dimensionless figure-of-merit ZT of each sample. In spite of the trade-off relation between the electrical conductivity and the thermal conductivity, the PEDOT:PSS infiltration process provides a 10% increment in the ZT value for both *p*- and *n*-type TE materials. The result is very encouraging because previously reported organic–inorganic hybrid composite materials showed low TE properties compared to that of original inorganic material.

Fig. 3 shows the resistance changes of the screen-printed TE films before and after PEDOT:PSS infiltration process as a function of the bending radius. The resistance values in this plot were normalized by the resistance of the flat sample to clearly see the relative difference after bending. The 400 nm-thick Cu film deposited by the thermal evaporation process on both sides of the sample was used as an electrode for the measurement. The resistances of unbent Bi_2Te_3 samples with and without PEDOT:PSS infiltration are 9.1 Ω and 9.2 Ω. The resistance of unbent Sb_2Te_3 samples is 2.0 Ω for both with and without PEDOT:PSS infiltration. The results show that both Bi_2Te_3 (Fig. 3a) and Sb_2Te_3 (Fig. 3b) samples with PEDOT:PSS infiltration maintain their resistance up to a bending radius of 3 cm, whereas the samples without PEDOT:PSS

infiltration show significant increases in their resistances as the bending radius becomes small. This result confirms that the flexibility of the screen-printed TE films is greatly enhanced by the PEDOT:PSS infiltration process. Such results can be explained that PEDOT:PSS plays a role of good electrical connector between clusters in the film during bending due to its high flexibility, which is supported by the SEM images in Fig. 1c and e.

Before TEG module fabrication, the area ratio of *n*-type and *p*-type TE legs must be optimized because each type of TE legs has different electrical and thermal properties. The optimum area ratio of A_n/A_p estimated by using Eq. (7) and the values in Table 1 is approximately 3. This theoretical result coincides well with the experimental result, as shown in Fig. 4 and Table 2. When the area ratio of A_n/A_p is 3, the Seebeck coefficient and output power density of the TEG module are maximized. The Seebeck coefficient of the TEG module with area ratio of 3 was 240.5 ± 4.2 μV K^{-1}. This value is almost the same as sum of the Seebeck coefficient of *n*-type and *p*-type TE legs in Table 1. Such results support that the area ratio of *n*-type and *p*-type TE legs must be optimized.

Fig. 5 shows output characteristics of a proto-type flexible TEG module fabricated with 7 TE couples using the techniques described above. A PI film was used as a flexible substrate and a

Table 3
Output characteristics of the fabricated flexible thermoelectric power generator module. The temperature of the cold side was maintained stably at 283 ± 1 K.

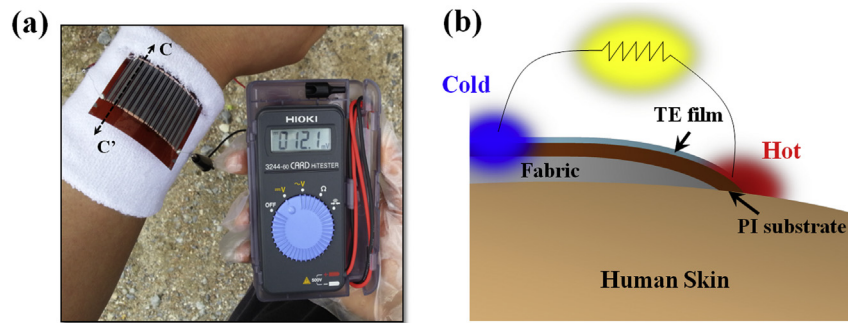| Temperature difference (K)	Hot side temperature (K)	Output voltage (mV)	Output power density (mW cm^{-2})
10	293	19.1 ± 1.9	0.06 ± 0.01
20	303	34.5 ± 1.7	0.19 ± 0.02
30	313	51.5 ± 1.7	0.42 ± 0.03
40	323	67.4 ± 1.7	0.74 ± 0.03
50	333	85.2 ± 1.7	1.22 ± 0.05

Fig. 6. (a) Performance demonstration of a flexible TEG module with 15 TE couples and the length of 30 mm, using the temperature difference between the body temperature and the ambient air temperature. The output voltage of the module using body heat was 12.1 mV at a temperature difference of about 5 K. (b) Cross section along with C–C'.

screen-printed Ag film was used for electrode (photograph, Fig. 5d). The area ratio of the *n*-type and *p*-type TE legs was adjusted to be 3 to obtain the highest output power density from the module. To reliably evaluate the output characteristics of the fabricated TEG module, the hot side temperature was ramped up, while the cold side temperature was kept constant (Fig. 5a). The temperature of the cold side was maintained stably at 10 ± 1 °C. Fig. 5b and Table 3 show the output voltage and output power density of the module as a function of temperature difference. The module has produced the output voltage of 85.2 mV and the output power density of 1.2 mW cm^{-2} at a 50 K temperature difference with a hot side temperature of 333 K. The mW-level output performance indicates that the fabricated TEG module has potential for utilization as an auxiliary power system for various low-power wearable mobile electronics. Fig. 5c shows the resistance changes of the module as a function of bending radius in the chain direction (A–A') and leg direction (B–B'). The internal resistance of the unbent (flat) TEG module is 145.2 Ω. The resistance of the flexible TEG module did not change up to a bending radius of 3 cm in either direction. Moreover, the module showed excellent bending fatigue strength (Fig. 5d), where the bending radius was fixed at 4 cm. Even after being bent 1000 times, the module exhibited little resistance changes within 3~6%. These results support that the flexible high-performance TEG module can be realized using a screen-printed inorganic TE film and organic conducting polymer hybrid composite.

The output performance of a flexible TEG module with 15 TE couples has also been demonstrated using the temperature difference between the body temperature and the ambient air temperature. Fig. 6a and b shows performance demonstration of the TEG module exploiting body heat and cross section along with C–C'. In this case, the length of the TE legs was designed to be 30 mm so that the cold side of the leg can be easily separated from the body. The output voltage of the module was 12.1 mV at a temperature difference of approximately 5 K. The results demonstrate that the flexible TEG module exploiting body heat can be used for various practical applications.

4. Conclusions

In conclusion, flexible high-performance TEG modules by using a screen-printed inorganic TE thick film and organic conducting polymer hybrid composite were successfully demonstrated. With this new approach, the micropores in the screen-printed TE film were filled with an organic conducting polymer, PEDOT:PSS. Incorporation of PEDOT:PSS into the screen-printed TE film significantly improved the flexibility of the film up to a bending radius of 3 cm without degradation of TE properties. Addition of PEDOT:PSS to the TE thick film increased both the electrical

conductivity and thermal conductivity, but resulted in a slight increment of the figure-of-merit ZT. The flexible TEG module fabricated by this technique has produced high output power density of 1.2 mW cm^{-2} at a 50 K temperature difference and showed excellent bending fatigue strength. The module also has additional advantages such as light weight and low fabrication cost compared to the conventional bulk TEG module. This work is expected to facilitate practical applications of flexible TEG modules for energy harvesting anywhere that a temperature difference can be exploited.

References

[1] Rowe DM. Thermoelectrics, an environmentally-friendly source of electrical power. Renew Energy 1999;16:1251–6.
[2] Snyder GJ, Toberer ES. Complex thermoelectric materials. Nat Mater 2008;7: 105–14.
[3] Gou X, Yang S, Xiao H, Ou Q. A dynamic model for thermoelectric generator applied in waste heat recovery. Energy 2013;52:201–9.
[4] Favarel C, Bédécarrats J-P, Kousksou T, Champier D. Numerical optimization of the occupancy rate of thermoelectric generators to produce the highest electrical power. Energy 2014;68:104–16.
[5] Chinese D, Meneghetti A, Nardin G. Diffused introduction of organic rankine cycle for biomass-based power generation in an industrial district: a systems analysis. Int J Energ Res 2004;28(11):1003–21.
[6] Kim Y, Kim C, Favrat D. Transcritical or supercritical CO$_2$ cycles using both low-and high-temperature heat sources. Energy 2012;43(1):402–15.
[7] Tuo H. Thermal-economic analysis of a transcritical rankine power cycle with reheat enhancement for a low-grade heat source. Int J Energ Res 2013;37(8): 857–67.
[8] Li G, Hwang Y, Radermacher R. Review of cold storage materials for air conditioning application. Int J Refrig 2012;35(8):2053–77.
[9] Li G, Hwang Y, Radermacher R, Chun H-H. Review of cold storage materials for subzero applications. Energy 2013;51:1–17.
[10] Li G, Liu D, Xie Y. Study on thermal properties of TBAB–THF hydrate mixture for cold storage by DSC. J Therm Anal Calorim 2010;102(2):819–26.
[11] Li G, Qian S, Lee H, Hwang Y, Radermacher R. Experimental investigation of energy and exergy performance of short term adsorption heat storage for residential application. Energy 2014;65:675–91.
[12] Li G. Review of thermal energy storage technologies and experimental investigation of adsorption thermal energy storage for residential application (Master thesis). College Park: University of Maryland; 2013.
[13] Lesage FJ, Pagé-Potvin N. Experimental analysis of peak power output of a thermoelectric liquid-to-liquid generator under an increasing electrical load resistance. Energ Convers Manage 2013;66:98–105.
[14] Francioso L, De Pascali C, Farella I, Martucci C, Cretì P, Siciliano P, et al. Flexible thermoelectric generator for ambient assisted living wearable biometric sensors. J Power Sources 2011;196:3239–43.

[15] Bubnova O, Khan ZU, Malti A, Braun S, Fahlman M, Berggren M, et al. Optimization of the thermoelectric figure of merit in the conducting polymer poly (3, 4-ethylenedioxythiophene). Nat Mater 2011;10:429—33.

[16] Piao M, Na J, Choi J, Kim J, Kennedy GP, Kim G, et al. Increasing the thermoelectric power generated by composite films using chemically functionalized single-walled carbon nanotubes. Carbon 2013;62:430—7.

[17] Zhang K, Zhang Y, Wang S. Enhancing thermoelectric properties of organic composites through hierarchical nanostructures. Sci Rep 2013;3.

[18] Jin Y, Nola S, Pipe KP, Shtein M. Improving thermoelectric efficiency in organic-metal nanocomposites via extra-low thermal boundary conductance. J Appl Phys 2013;114:194303.

[19] Coates NE, Yee SK, McCulloch B, See KC, Majumdar A, Segalman RA, et al. Effect of interfacial properties on polymer—nanocrystal thermoelectric transport. Adv Mater 2013;25:1629—33.

[20] Du Y, Cai K, Chen S, Cizek P, Lin T. Facile preparation and thermoelectric properties of Bi_2Te_3 based alloy nanosheet/PEDOT: PSS composite films. ACS Appl Mater Interfaces 2014;6:5735—43.

[21] Lee H-B, Yang HJ, We JH, Kim K, Choi KC, Cho BJ. Thin-film thermoelectric module for power generator applications using a screen-printing method. J Electron Mater 2011;40:615—9.

[22] Lee HB, We JH, Yang HJ, Kim K, Choi KC, Cho BJ. Thermoelectric properties of screen-printed ZnSb film. Thin Solid Films 2011;519:5441—3.

[23] We JH, Kim SJ, Kim GS, Cho BJ. Improvement of thermoelectric properties of screen-printed Bi_2Te_3 thick film by optimization of the annealing process. J Alloy Compd 2013;552:107—10.

[24] Kim SJ, We JH, Kim JS, Kim GS, Cho BJ. Thermoelectric properties of p-type Sb_2Te_3 thick film processed by a screen-printing technique and a subsequent annealing process. J Alloy Compd 2014;582:177—80.

[25] Chang K-C, Jeng M-S, Yang C-C, Chou Y-W, Wu S-K, Thomas MA, et al. The thermoelectric performance of poly (3, 4-ethylenedi oxythiophene)/poly (4-styrenesulfonate) thin films. J Electron Mater 2009;38:1182—8.